Oscillation-free source term inversion of atmospheric radionuclide releases with joint model bias corrections and non-smooth competing priors

Sheng Fang[1], Xinwen Dong[1], Shuhan Zhuang[1], Zhijie Tian[2], Tianfeng Chai[3,4], Yuhan Xu[1], Yungang Zhao[5,6], Li Sheng[7], Xuan Ye[1], Wei Xiong[1]**

[1]Institute of Nuclear and New Energy Technology, Collaborative Innovation Centre of Advanced Nuclear Energy Technology, Key Laboratory of Advanced Reactor Engineering and Safety of Ministry of Education, Tsinghua University, Beijing 100084, China.

[2]China Institute for Radiation Protection, Taiyuan 030006, China.

[3]NOAA Air Resources Laboratory (ARL), NOAA Center for Weather and Climate Prediction, 5830 University Research Court, College Park, MD 20740, USA.

[4]Cooperative Institute for Climate and Satellites, University of Maryland, College Park, MD 20740, USA.

[5]Key Laboratory of Beam Technology of Ministry of Education, College of Nuclear Science and Technology, Beijing Normal University, Beijing 100875, China.

[6]CTBT Beijing National Data Centre and Beijing Radionuclide Laboratory, Beijing 100085, China.

[7]CMA Earth System Modeling and Prediction Center (CEMC), Beijing 100081, China.

*Corresponding author. Email: yexuan@tsinghua.edu.cn (Xuan Ye); xwthu@tsinghua.edu.cn (Wei Xiong).

Abstract: The source term of atmospheric radionuclide releases is essential for the hazardous consequence assessment and emergency response. However, the artificial release oscillations in the source term estimate remain a fundamental challenge and may deliver misleading information, because of the unavoidable model biases and observation uncertainties. We propose a new method that removes oscillations while recovering the release details. This method explicitly corrects the model biases using the joint correction model and compensates the observation uncertainties through non-smooth competing priors that involve two rival functions. The new priors better model the unsteady feature of the radionuclide releases and distinguish the true releases from oscillations, enabling release-preserving oscillation removal. We extend the projected alternating minimization algorithm for an efficient solution. The method achieves oscillation-free and nearly perfect profiles for real releases of the Perfluoro-Methyl-Cyclo-Hexane on continental and regional scales, and the radionuclide ^{41}Ar on a local scale, outperforming state-of-the-art and very recent methods. The sensitivities to model inputs and key parameters are also investigated. Robust performance is exhibited under emissions of both radioactive and non-radioactive substances, different meteorological inputs and numbers of observations, paving the way for identifying dynamic atmospheric radionuclide releases at multiple scales, especially when the release status is unknown.

Keywords: inverse modeling, atmospheric emission, hazardous substance, model bias correction, observation uncertainties

1. Introduction

The atmospheric release of radionuclides is a widely-concerned hazard to both the environment and the public health, which raises global public interest in a series of release events, such as the 1986 Chernobyl accident [1], 2011 Fukushima accident [2], 2017 Ru-106 leakage [3] and the recent fire-induced releases in and around the Chernobyl exclusion zone [4]. The source term, i.e., the temporal profile, of radionuclide releases in these events is important for consequence assessment and emergency response. The inversion method retrieves the release profile by comparing environmental observations with the simulation results of an atmospheric dispersion model (ADM). Compared with forward methods, which attempt to model the emission procedure, a key advantage of the inversion method is that environmental observations are more accessible than data regarding the emission process. This makes the inversion method extremely useful in situations where the emission process cannot be measured or derived with the forward method, such as the aforementioned events.

In practice, the artificial release oscillations in the estimated profile remain a fundamental challenge in applying the inversion method, as these may be mixed with the true release to produce misleading results. A critical source of these oscillations is the mismatch between observations and ADM simulations, i.e., the model biases [5], which come from the inevitable uncertainties in both the meteorological inputs [6] and the ADM [7]. The handling of these model biases is important for oscillation removal, and can generally be divided into two families: explicit correction and implicit compensation.

Explicit methods simultaneously correct the model biases and estimate the release profile, such as the direct refinement of the ADM parameters [8–10], joint correction of the combined effects of model biases [5,7], and spatiotemporal displacement correction of model predictions

[11]. Among these, joint correction models that correct the combined model biases have achieved nearly perfect inversion with high-quality observations in two wind tunnel experiments [5,7]. However, explicit correction has more unknown variables than standard inversion, leading to increased ill-posedness and further amplification of observation uncertainties. For this reason, the displacement correction method still exhibits considerable oscillations in real scenarios where observation uncertainties exist, even if the advanced sparsity and smoothness priors are used to constrain the solution [11].

Implicit methods compensate the model biases using regularization, which adds additional *a priori* information of the release profile (i.e., the prior) into the inversion, such as the statistical distribution [10,12–17], smoothness, sparsity [13,18–20], and *a priori* profile [14]. Through appropriate parameterization, the implicit approach tips the solution toward the prior and reduces its dependence on the biased model and the observations, so that the influence of the observation uncertainties and the oscillations are reduced. However, this strategy increases the prior error, which results from the inevitable discrepancy between the prior and the true release profile. Most of the existing priors assume that the release is smooth with limited overall amplitude or number of releases [14], but the radionuclide release is unsteady and unsmooth, involving sharp peaks and constant releases [21,22]. Because of this discrepancy, the implicit method may deteriorate information regarding the true releases when removing oscillations and may fail to recover the release details.

Therefore, it is still difficult for both explicit and implicit methods to balance oscillation removal with release recovery in a real case, where both significant model biases and observation uncertainties exist. Because of this dilemma, perfect inversion of real atmospheric emissions remains an open problem.

Herein, we propose a new inversion method that combines the joint correction model and a new regularization scheme using two competing non-smooth priors. The joint model explicitly corrects the model biases, while the new priors adaptively compensate the observation uncertainties. The two priors respectively encourage piecewise-constant releases and temporal sparsity in the estimated profile, offsetting each other's side effects and enabling a better description of the unsteady and unsmooth features of the radionuclide releases. Through their competition, the priors can distinguish the true releases from oscillations and can simultaneously achieve both oscillation removal and release recovery. We extend the projected alternating minimization (PAM) [23] algorithm to stably solve the proposed regularized joint correction model. The proposed method is validated on three different field experiments at different scales, which are the first European Tracer Experiment (ETEX-I, continental-scale) [24] and the Cross-Appalachian Tracer Experiment (CAPTEX, regional-scale) [25] with emissions of Perfluoro-Methyl-Cyclo-Hexane (PMCH), and the SCK-CEN experiment (local-scale) [26] with emissions of the radionuclide ^{41}Ar. The performance of this method is compared with the least-square with the adaptive prior covariance (LSAPC) method [12] and its successor BiasCorr-LSAPC [11], which are state-of-the-art methods. Its sensitivity to the meteorological inputs and the number of observations is investigated. The key parameters as well as the roles of each prior and the PAM algorithm are also discussed.

2. Materials and methods

2.1. Standard inversion model

The basic relationship between observations and the release profile of atmospheric emissions can be described as:

$$\boldsymbol{\mu} = \mathbf{H}\boldsymbol{\sigma} + \boldsymbol{\varepsilon} \quad (1)$$

where $\boldsymbol{\mu} \in \mathbf{R}^m$ is a vector of spatiotemporal observations and $\boldsymbol{\sigma} \in \mathbf{R}^n$ is an unknown vector containing the release profile over N time steps. $\boldsymbol{\varepsilon} \in \mathbf{R}^m$ represents the possible errors. $\mathbf{H}^{\boldsymbol{m}\times\boldsymbol{n}}$ is the source–receptor matrix, describing the sensitivity of each observation to a unit release rate, and $\mathbf{H}\boldsymbol{\sigma}$ is equivalent to running an ADM with $\boldsymbol{\sigma}$ as the input release profile. Because $\mathbf{H}$ is calculated using such a model, it inherits the biases that are inevitable in ADMs. Consequently, $\mathbf{H}\boldsymbol{\sigma}$ may deviate from the true dispersion and will not necessarily match the observations on the left-hand side of Eq. (1), even if $\boldsymbol{\sigma}$ is the true release profile. The standard method assumes a certain distribution of $\boldsymbol{\varepsilon}$, and adds a corresponding regularization term to the inversion to implement this prior knowledge. For instance, the most widely-used prior knowledge assumes that $\boldsymbol{\varepsilon}$ follows a Gaussian distribution, which leads to the following Tikhonov regularization.

$$\boldsymbol{\sigma} = \underset{\boldsymbol{\sigma}}{\operatorname{argmin}} \left\{ \frac{1}{2}(\boldsymbol{\mu} - \mathbf{H}\boldsymbol{\sigma})^T \mathbf{R}^{-1} (\boldsymbol{\mu} - \mathbf{H}\boldsymbol{\sigma}) + \frac{1}{2}\boldsymbol{\sigma}^T \mathbf{P}^{-1} \boldsymbol{\sigma} \right\} \quad (2)$$

where $\mathbf{R}$ and $\mathbf{P}$ represent the covariance matrices of the observation error and the prior error, respectively. However, the standard approach does not update $\mathbf{H}$, so this mismatch is not corrected and may lead to unrealistic oscillations in the solution.

2.2. Joint correction model

The joint correction model explicitly corrects the mismatch that resides within $\mathbf{H}$ in the standard inversion model, while retrieving the release profile at the same time. This is achieved by adding a diagonal matrix of correction coefficients $\mathbf{W}$ to Eq. (1), in which every diagonal element $w_i (i = 1,2,\cdots,m)$ separately corrects the ADM simulation for a single observation. The resultant joint correction model is formulated as:

$$\boldsymbol{\mu} = \mathbf{W}\mathbf{H}\boldsymbol{\sigma} + \boldsymbol{\varepsilon} = \begin{bmatrix} w_1 & & & \\ & w_2 & & \\ & & \ddots & \\ & & & w_m \end{bmatrix} \begin{bmatrix} \mathbf{H}_1\boldsymbol{\sigma} \\ \mathbf{H}_2\boldsymbol{\sigma} \\ \vdots \\ \mathbf{H}_m\boldsymbol{\sigma} \end{bmatrix} + \boldsymbol{\varepsilon} \quad (3)$$

where $\mathbf{H}_i$ is the i-th row of $\mathbf{H}$ and $\mathbf{H}_i\boldsymbol{\sigma}$ is the model simulation for the i-th observation. In Eq. (3), both $\mathbf{W}$ and $\boldsymbol{\sigma}$ are unknown variables. Hence, Eq. (3) is much more difficult to solve than Eq. (1) and additional prior knowledge has to be incorporated to obtain a reliable solution. In a previous study [5], a new form of prior knowledge was proposed for solving $\mathbf{W}$, whereby the center of the diagonal elements of $\mathbf{W}$ is assumed to be a constant, and the regular Gaussian prior is employed for solving $\boldsymbol{\sigma}$. This combination achieved substantially improved inversion accuracy in two wind tunnel experiments [5,7], in which the release rate was constant and the quality of observations was high. However, the joint correction model is more ill-posed than the standard method, because it introduces more unknown variables (i.e. $\mathbf{W}$ in Eq. (3)). For this reason, the joint correction model is more sensitive to observation uncertainties than the standard method. Unfortunately, large uncertainties may exist in the observations in a real dispersion case, aggravating the artificial oscillations in the solution of the joint correction model. This sensitivity has been observed in a previous study that also introduces additional unknown variables for spatiotemporal displacement correction [11], even though the advanced sparsity and smoothness prior is implemented for oscillation reduction.

2.3. Regularized joint correction model with non-smooth competing priors

Noticing that the radionuclide releases are unsteady and unsmooth [21,22], we propose the use of two non-smooth competing priors to better model these features and to constrain the joint correction model. The first is the sparsity prior which assumes that the releases are sparse in the temporal domain. The sparsity prior encourages a limited number of sharp peaks and reduces the number of small releases in the solution (Fig. 1A), which the latter is mainly determined by the artificial oscillations. To implement this prior, we add the term $||\boldsymbol{\sigma}||_1$ as the first regularization term, where $||\cdot||_1$ denotes the L1-norm [27]. A side effect of the sparsity prior is that it reduces the duration of the true releases. To offset this, a second prior is added which assumes that the release profile is piecewise-constant. This assumption encourages constant releases with finite durations (Fig. 1B), which preserves the release duration and reduces the frequent changes of releases, i.e., the oscillations. To implement the piecewise-constant prior, we add the total variation (TV) term $||\nabla\boldsymbol{\sigma}||_1$ as a second regularization term, where ∇ is the derivative operator. The combination of these two priors enables the modeling of both the sharp peaks and constant releases in the regularization, which better preserves the unsteady and unsmooth features of the radionuclide releases in the solution. Because both priors suppress oscillations, this combination can simultaneously remove oscillations while recovering release details. With the non-smooth competing priors, Eq. (3) can be solved under the framework of regularization as:

$$\mathbf{W},\boldsymbol{\sigma} = \underset{\mathbf{W},\boldsymbol{\sigma}}{\operatorname{argmin}}\left\{\frac{1}{2}\left||\mathbf{WH}\boldsymbol{\sigma} - \boldsymbol{\mu}|\right|_2^2 + \lambda(\alpha\left||\boldsymbol{\sigma}|\right|_1 + (1-\alpha)\left||\nabla\boldsymbol{\sigma}|\right|_1)\right\}$$

$$\boldsymbol{s.t.}\ \mathbf{W} >= 0,\ \text{center}(\text{diag}(\mathbf{W})) = \text{Const.} \qquad (4)$$

where λ is the regularization parameter; the second line of Eq. (4) states the non-negativity and center constraints on the correction coefficients matrix $\mathbf{W}$. α is the weight for the L1-norm regularization. By choosing an appropriate weight α, a good balance can be achieved between the two terms, enabling simultaneous oscillation removal and release recovery in solving Eq. (4).

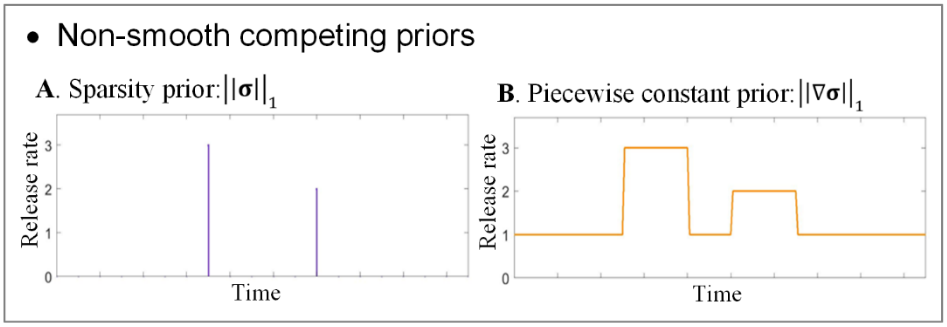

Figure 1. Illustration of the features of non-smooth competing priors. (A) the sparsity prior $||\boldsymbol{\sigma}||_1$; (B) the piecewise constant prior $||\nabla\boldsymbol{\sigma}||_1$.

2.4. Projected alternating minimization algorithm

An effective strategy for solving Eq. (4) is to split it into two subproblems with only a single unknown variable using the fact that **W** is a diagonal matrix:

$$\boldsymbol{\sigma} \text{ subproblem:} \quad \boldsymbol{\sigma} = \underset{\mathbf{W},\boldsymbol{\sigma}}{\operatorname{argmin}}\left\{\frac{1}{2}||\mathbf{WH}\boldsymbol{\sigma} - \boldsymbol{\mu}||_2^2 + \lambda(\alpha||\boldsymbol{\sigma}||_1 + (1-\alpha)||\nabla\boldsymbol{\sigma}||_1)\right\} \tag{5}$$

$$\tilde{\mathbf{w}} \text{ subproblem:} \quad \tilde{\mathbf{w}} = \underset{\mathbf{W},\boldsymbol{\sigma}}{\operatorname{argmin}}\left\{\frac{1}{2}||\mathbf{WH}\boldsymbol{\sigma} - \boldsymbol{\mu}||_2^2\right\} \;\; \boldsymbol{s.t.}\; \tilde{\mathbf{w}}>=0,\ \text{center}(\tilde{\mathbf{w}}) = c. \tag{6}$$

Here, $\tilde{\mathbf{w}} = \text{diag}(\mathbf{W})$ is a vector comprising the diagonal elements of **W**, $\tilde{\mathbf{H}} = \text{diag}(\mathbf{H}_i\boldsymbol{\sigma})$, $i = 1,2,\cdots,m$, $\mathbf{H}_i$ is the i-th row of **H**, and $\tilde{\mathbf{H}}$ is a diagonal matrix with diagonal elements $\mathbf{H}_i\boldsymbol{\sigma}$. And c is a constant constraint posed to the center of the correction coefficients. The alternating minimization algorithm [5,7] solves the two subproblems sequentially in each iteration. Although satisfactory accuracy has been achieved in wind tunnel experiments, the alternating minimization algorithm prefers a smooth solution and may not preserve the sharp jumps of the estimate [28]. Thus, the PAM algorithm [23] is used to solve Eq. (4) in this study, as this has the ability to preserve sharp changes in the estimates. PAM also alternates between the two subproblems in each iteration, but does not pursue complete (final) solutions. Instead, in each iteration, PAM updates the solution of the two subproblems by a small step based on the gradients of Eqs. (5) and (6), respectively.

In our P̲rojected A̲lternating M̲I̲nimization with L̲1-norm and T̲otal variation regularization (PAMILT) algorithm, each iteration consists of three sequential steps: update of the release profile, update of the correction coefficients, and the constraining of the correction coefficients. The two update steps adjust the corresponding current estimate with a single gradient descent step. The constraining step imposes the constraints in the second line of Eq. (4).

The update formulae for the two subproblems based on the gradient descent method are as follows:

$$\boldsymbol{\sigma}^{\mathrm{k}} \leftarrow \boldsymbol{\sigma}^{\mathrm{k}-1} - \delta\left[(\mathbf{W}^{\mathrm{k}-1}\mathbf{H})^{\mathrm{T}} \cdot \left(\mathbf{W}^{\mathrm{k}-1}\mathbf{H} \cdot \boldsymbol{\sigma}^{\mathrm{k}-1} - \mathbf{f}\right) - \lambda\left(\alpha \cdot \frac{\nabla\boldsymbol{\sigma}^{\mathrm{k}-1}}{\left\|\nabla\boldsymbol{\sigma}^{\mathrm{k}-1}\right\|_2} + (1-\alpha) \cdot \nabla \cdot \frac{\nabla\boldsymbol{\sigma}^{\mathrm{k}-1}}{\left\|\nabla\boldsymbol{\sigma}^{\mathrm{k}-1}\right\|_2}\right)\right] \quad (7)$$

$$\widetilde{\mathbf{w}}^{\mathrm{k}} \leftarrow \widetilde{\mathbf{w}}^{\mathrm{k}-1} - \delta\left[(\mathbf{H}\boldsymbol{\sigma}^{\mathrm{k}})^{\mathrm{T}} \cdot \left(\mathbf{H}\boldsymbol{\sigma}^{\mathrm{k}} \cdot \widetilde{\mathbf{w}}^{\mathrm{k}-1} - \mathbf{f}\right)\right] \quad (8)$$

where δ is the update step. After these two steps, the positivity constraints in Eq. (6) are applied to the estimated correction coefficients $\widetilde{\mathbf{w}}$ in the projection step:

$$\widetilde{\mathbf{w}}^{\mathrm{k}} = \max\{\widetilde{\mathbf{w}}^{\mathrm{k}}, 0\},\ \widetilde{\mathbf{w}}^{\mathrm{k}} = \widetilde{\mathbf{w}}^{\mathrm{k}}/\mathrm{center}(\widetilde{\mathbf{w}}^{\mathrm{k}})*c. \quad (9)$$

The center of the correction coefficients is estimated using the univariate Minimum Covariance Determinant (MCD) method [5].

A flowchart of PAMILT, related parameter settings, and initializations are presented in Table 1. The initial release profile is estimated as a zero vector, whereas that of the correction coefficients is calculated based on observations and model simulations using a constant release profile with unit rates. The main parameters of the proposed method are the regularization parameter λ, the ratio between the TV and L1-norm terms α, and the center constraint of the correction coefficients c. In this study, α and c are empirically determined to be 0.1 and 0.001, respectively.

Table 1. Flow of the proposed method for solving $\boldsymbol{\sigma}$ and $\widetilde{\mathbf{w}}$.

Set initial values: $\boldsymbol{\sigma}^0 = 0\mathbf{I}$, $\widetilde{\mathbf{w}}^0 = \mathbf{y}_{\mathrm{obs}}/(\mathbf{H} \cdot 1\mathbf{I})$

Iterate $k = 1,2,\cdots$ until $\left\|\boldsymbol{\sigma}^{\mathrm{k}} - \boldsymbol{\sigma}^{\mathrm{k-1}}\right\|_2 / \left\|\boldsymbol{\sigma}^{\mathrm{k-1}}\right\|_2 < 10^{-3}$

or $\|\widetilde{\mathbf{w}}^{k} - \widetilde{\mathbf{w}}^{k-1}\|_2 / \|\widetilde{\mathbf{w}}^{k-1}\|_2 < 10^{-10}$

Form $\mathbf{W}^{k-1}$ matrix: $\mathbf{W}^{k-1} = \mathrm{diag}(\widetilde{\mathbf{w}}^{k-1})$

$\boldsymbol{\sigma}$-step:

Update $\boldsymbol{\sigma}^{k}$ with $\mathbf{W}^{k-1}$ using Eq. (7)

$\widetilde{\mathbf{w}}$-step:

Update $\widetilde{\mathbf{w}}^{k}$ with $\boldsymbol{\sigma}^{k}$ using Eq. (8)

Projection step:

Update $\widetilde{\mathbf{w}}^{k} = \max\{\widetilde{\mathbf{w}}^{k}, 0\}$

Normalization step:

Compute the center of $\widetilde{\mathbf{w}}^{k}$: $t^{k} = MCD(\widetilde{\mathbf{w}}^{k})$

Normalize $\widetilde{\mathbf{w}}^{k}$: $\widetilde{\mathbf{w}}^{k} = \widetilde{\mathbf{w}}^{k}/t^{k} * c$

2.5. Field experiments

The proposed method was validated against three field experiments at continental, regional, and local scales respectively. The continental-scale experiment is the ETEX-I [29], of which a total of 340 kg PMCH was released on October 23, 1994 and the corresponding observations were acquired across Europe. The observation network of ETEX-I comprises 168 ground sites (Fig. 2A) and covers 17 European countries [24]. The sampling action lasted 90 h with intervals of 3 h, and ultimately provided a total of 3104 usable observations.

The regional-scale experiment is the 2nd release of the CAPTEX [25], of which 201 kg of PMCH was released from 17:05 to 20:05 on September 25, 1983. The locations of 68 observation sites are up to 1000 km from the release position (Fig. 2B). These sites provided 375 observations from the start of the experiment until 00:00 on September 27, 1983 [25].

The local-scale experiment is the SCK-CEN experiment on October 4, 2001, of which the radionuclide ^{41}Ar was released from a stack [26]. Figure 2C presents the four radioactivity observation sites involved in inversion, which are all within 400 m of the release. A total of 592 fluence rate observations of γ rays were collected using an array of NaI(Tl) detectors.

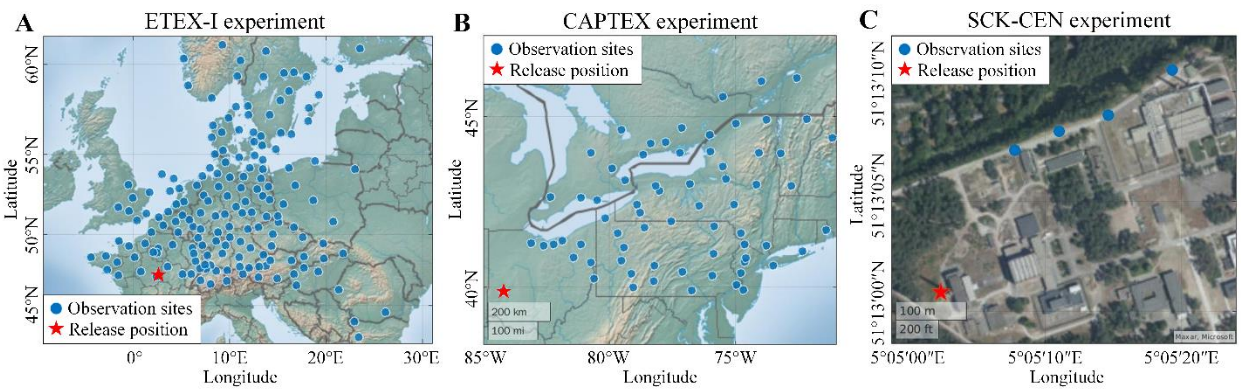

Figure 2. Monitoring networks (blue dots) and release positions (red star) of three different field experiments. (A) the ETEX- I experiment; (B) the CAPTEX experiment; (C) the SCK-CEN experiment.

2.6. Source–receptor matrices calculation

For consistency with previous studies, the four source–receptor matrices of ETEX-I experiment used in a previous study [18] were adopted here, which were kindly shared by Adam Lukas and Ondrej Tichy at http://staff.utia.cas.cz/adam/research.html. These matrices (3104 × 120) were calculated using HYSPLIT 4 [18] with two different types of meteorological data (the 40-year re-analysis (ERA-40) and the continuously updated ERA-Interim re-analysis) and two different time step settings [12,18], which are referred to as ERA-40 A, ERA-40 B, ERA-Interim A, and ERA-Interim B. More details of the matrix calculation can be found in the references [12,18].

As for the CAPTEX experiment, the FLEXPART-WRF model (Version 3.3.2) was used to calculate the source–receptor matrix (2179 × 288). This software is available at https://www.flexpart.eu/. The raw meteorological data of CFSR were downloaded from https://rda.ucar.edu/. These data were processed into input meteorological fields using the Weather Research and Forecasting (WRF) numerical model, of which the spatial domain covers [69.5° W, 85.0° W], [38.5° N, 47.0° N] and has 15 vertical levels from 0–8000 m.

The SWIFT-RIMPUFF model was used to calculate the source–receptor matrix (592 × 148) of SCK-CEN experiment with the onsite meteorological observations and model parameters reported in a previous study [30].

2.7. Sensitivity analysis

2.7.1. Sensitivity to the meteorological inputs

Meteorological inputs affect the ADM parameter settings and pose challenges for inversion. Besides the ERA-40 B case, the performance of PAMILT was also compared with the LSAPC method for three other ETEX-I scenarios involving different meteorological inputs and parameter settings, i.e., the ERA-40 A, ERA-Interim A, and ERA-Interim B. The estimated release profiles were involved in comparison, as well as the maximal model biases at each site before and after PAMILT correction.

2.7.2. Sensitivity to the number of observation sites

The performance of PAMILT was evaluated with respect to the number of observation sites based on the ERA-40 B case of the ETEX-I experiment. Four ratios for random selection of the observation sites were considered for estimating the release profiles using LSAPC and PAMILT, which are 12.5%, 25%, 50%, and 75%.

2.7.3. Sensitivity to the regularization parameter

The sensitivity of the proposed method to the regularization parameter λ was investigated by estimating the release profiles using a geometric range of λ for each field experiment. The relative inversion error was calculated using Eq. (10) to reveal the influence of λ on the accuracy.

$$\text{Relative inversion error} = \|\sigma_{\mathbf{true}} - \sigma_{\mathrm{e}}\|_{\mathbf{2}} / \|\sigma_{\mathbf{true}}\|_{\mathbf{2}} \quad (10)$$

where, $\boldsymbol{\sigma}_{\mathrm{true}}$ is the true release rate and $\boldsymbol{\sigma}_{\mathbf{e}}$ is the estimated release profile.

2.7.4. Sensitivity to the ratio of two regularization terms

The behavior of the regularization is controlled by the ratio α between the L1-norm and TV terms, which ensures the simultaneous preservation of both the sharp changes and the steady state of the profile. The proposed method was applied to the ERA-40 B case of the ETEX-I experiment with values of α ranging from 0.1 to 0.9. The estimated release profiles were compared with the true release profiles, revealing the effect of the two competing priors with different weights.

2.7.5. Sensitivity to the center constraint value

The sensitivity of the proposed method to the center constraint c was performed with a geometric range of center constraint values from 10^{-4} to 10^{2}, based on the ERA-40 B case of the ETEX-I experiment. The relative inversion error was calculated for selecting an optimal c, whereas the distributions of the correction coefficients and release profiles are accessed to investigate the influence of this constraint on inversion.

2.8. Quantitative evaluation

2.8.1. Model biases calculation

To quantify the discrepancies between the observations and the model simulations, the model biases of ADMs before correction were calculated as:

$$e_i = \mu_i / (\mathbf{H}_i \cdot \boldsymbol{\sigma}_{\mathrm{true}}) \quad (11)$$

where μ_i is the i-th observation, e_i is the bias for μ_i, $\mathbf{H}_i$ is the i-th row of the source–receptor matrix $\mathbf{H}$, and $\boldsymbol{\sigma}_{\mathrm{true}}$ is the true release rate. After correction, the model biases were calculated as:

$$e_i = \mu_i / (\mathbf{W} \cdot \mathbf{H}_i \cdot \boldsymbol{\sigma}_{\mathrm{e}}) \quad (12)$$

where, $\boldsymbol{\sigma}_{\mathrm{e}}$ is the estimated release profile. Equations (11) and (12) can be viewed as the ratio between every observation and the corresponding model simulation, where $e_i = 1$ indicates perfect agreement, $e_i > 1$ indicates underestimation, and $e_i < 1$ indicates overestimation

2.8.2. Comparison of observations and model simulations

The model simulations at the observation sites using an estimated profile $\boldsymbol{\sigma}_{\mathrm{e}}$ were calculated via:

$$\mathbf{y}_{\mathrm{e}} = \mathbf{H} \cdot \boldsymbol{\sigma}_{\mathrm{e}} \quad (13)$$

where $\boldsymbol{\sigma}_{\mathrm{e}}$ represents the LSAPC profile or PAMILT profile. When with the correction function $\mathbf{W}$, Eq. (13) can be written as:

$$\mathbf{y}_{\mathrm{e}} = \mathbf{W} \cdot \mathbf{H} \cdot \boldsymbol{\sigma}_{\mathrm{e}} \quad (14)$$

To investigate the discrepancy between the observations $\mathbf{y}_{\mathrm{o}}$ and estimates $\mathbf{y}_{\mathrm{e}}$ at each site quantitatively, the factor of 2/5 (FAC2/5), fractional bias (FB), normalized mean square error (NMSE), and Pearson correlation coefficient (PCC) were used as statistical metrics. These are defined as:

$$\mathrm{FAC2} = \text{fraction of data for which } 0.5 \le \frac{\mathrm{y_e}}{\mathrm{y_o}} \le 2.0 \quad (15)$$

$$\mathrm{FAC5} = \text{fraction of data for which } 0.2 \le \frac{\mathrm{y_e}}{\mathrm{y_o}} \le 5.0 \quad (16)$$

$$\mathrm{FB} = 2(\overline{\mathrm{y_e}} - \overline{\mathrm{y_o}}) / (\overline{\mathrm{y_e}} + \overline{\mathrm{y_o}}) \quad (17)$$

$$\mathrm{NMSE} = \overline{(\mathrm{y_e} - \mathrm{y_o})^2} / (\overline{\mathrm{y_e}} \cdot \overline{\mathrm{y_o}}) \quad (18)$$

$$\mathrm{PCC} = \overline{(\mathrm{y_o} - \overline{\mathrm{y_o}})(\mathrm{y_e} - \overline{\mathrm{y_e}})} / (D_{\mathrm{e}} \cdot D_{\mathrm{o}}) \quad (19)$$

where $\overline{y}$ denotes the average value and D_e, D_o are the standard deviations of simulations and observations, respectively.

3. Results and discussion

3.1. Results for three field experiments

Figure 3A displays the maximal model biases at each observation site for the ETEX-I experiment. Without correction, most of the maximal model biases are above 10^8, indicating noticeable model biases in the ADM. After PAMILT correction, the maximal model biases are reduced to around 10^6 at most of the sites. The statistics in the lower-left corner indicate that PAMILT reduces the average of the maximal model biases by 30.3% and reduces the variance by 11.6%, which confirms its effectiveness in correcting model biases.

Figure 3B compares the release profile estimates of the state-of-art LSAPC method [12] and PAMILT. LSAPC recovers the sharp changes of the release rates at the start and end times of the release, and the major releases are within the time window of the true releases. However, there are oscillations in the release window, ranging from 1.3% to 337.2% of the true release rate. In addition, there is a noticeable artificial release of 4 h outside the true release window. In comparison, PAMILT not only successfully recovers the sharp release changes near the boundary of the release window, but also retrieves the steady release phase without any oscillations. Outside the release window, the PAMILT profile does not indicate any releases, which is in perfect agreement with the actual scenario. With respect to the total release, PAMILT shows a slight underestimation of about 13.4%, compared with up to 24.8% for LSAPC.

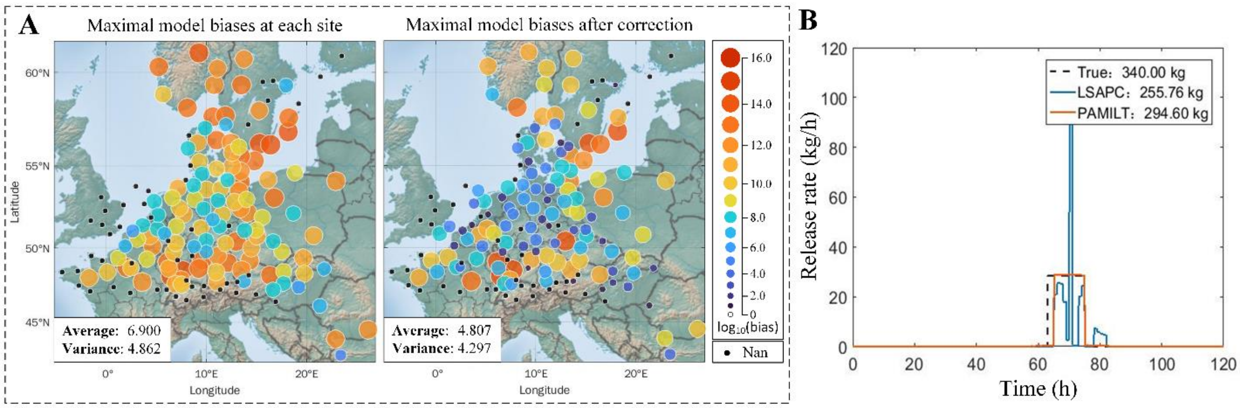

Figure 3. Inversion results for the ETEX-I experiment (ERA-40 B case). (A) Maximal model biases at each site before and after PAMILT correction; (B) comparison of the LSAPC and PAMILT estimates.

Figure 4A compares the maximal model biases before and after PAMILT correction of different observation sites in CAPTEX. PAMILT reduces the maximal model biases by two orders of magnitude, from $10^{5.8}$ to $10^{3.5}$, compared with the biases of the ADM before correction. The average and variance are reduced by 8.3% and 14.5%, respectively. Referring to the source term inversion, both methods avoid artificial releases outside the release window. The LSAPC profile shows a single sharp release, with the instant release rate overestimated by 104.7% and the release duration underestimated by 82.4% (Fig. 4B). PAMILT accurately recovers the start time, sharp increase, and steady phase of the release, though it overestimates the release duration by 0.83 h. As for the total release, LSAPC produces an underestimation of 89.1%, whereas PAMILT gives an overestimation of about 31.76%.

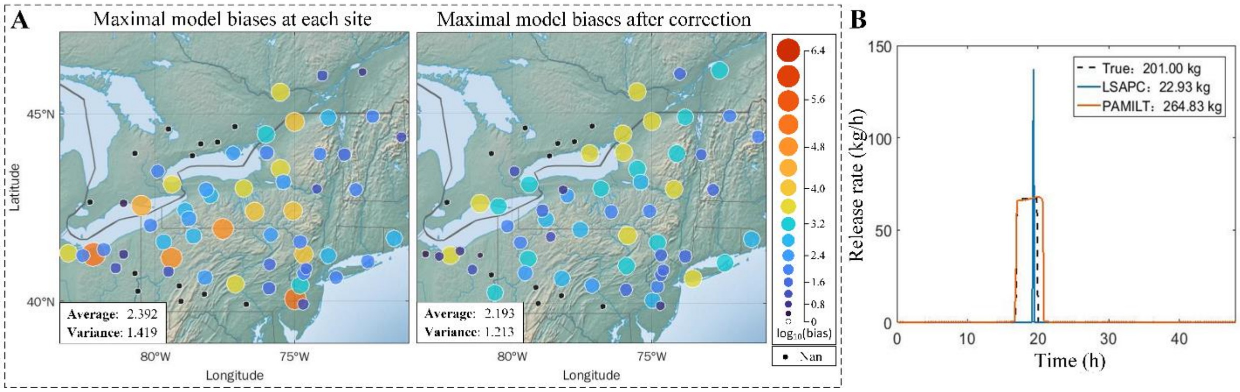

Figure 4. Inversion results for the CAPTEX experiment. (A) Maximal model biases at each site before and after PAMILT correction; (B) comparison of the LSAPC and PAMILT estimates.

The local-scale validation results are displayed in Fig. 5. The maximal model biases at these sites were around $10^{0.9}$ before correction, dropping to $10^{0.3}$ after PAMILT correction (Fig. 5A). The PAMILT profile of ^{41}Ar avoids the oscillations in the LSAPC profile and the release rate at the steady phase matches the true release rate exactly (Fig. 5B). PAMILT also produces a sharper increase at the start time of the release, whereas LSAPC gives better results at the end time. Both methods exhibit a delay in the start time of the release (about 1.67 h). PAMILT underestimates the total release by 23.14%, whereas LSAPC gives an underestimation of 44.67%.

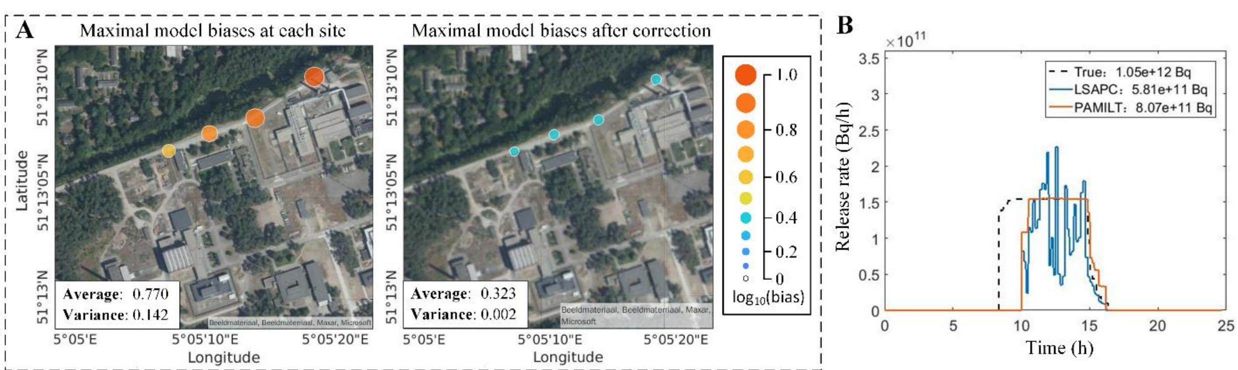

Figure 5. Inversion results for the SCK-CEN experiment. (A) Maximal model biases at each site before and after PAMILT correction; (B) comparison of the LSAPC and PAMILT estimates.

Table 2 summarizes the comparison between observations and model simulations for the three experiments using different release profile estimates. For both the ETEX-I and CAPTEX experiments, the PAMILT simulation without correction shows similar metrics as the LSAPC simulation. After correction, the PAMILT simulation exhibits noticeably improved FAC2/5s and PCCs than the LSAPC simulation. For the SCK-CEN experiment, the FAC5/2 of the PAMILT simulation without correction is better than that of the LSAPC simulation, whereas the PCC is slightly worse. With the correction, the FAC5/2 and PCC of PAMILT are noticeably improved and exceed those of the LSAPC. These metrics indicate the superior performance of PAMILT in the test cases, though the FBs are slightly worse than those of the LSAPC.

Table 2. Summary of performance measures for three experiments using different methods. The metrics for LSAPC, PAMILT without correction (PAMILT^1), and PAMILT with correction (PAMILT^2) are included.

Experiment	Method	FAC5	FAC2	FB	PCC
ETEX-I ERA-40 B	LSAPC	0.23	0.20	1.94	0.71
	PAMILT^1	0.23	0.20	1.95	0.67
	PAMILT^2	0.72	0.71	2.00	0.73
CAPTEX	LSAPC	0.51	0.48	1.14	0.76
	PAMILT^1	0.50	0.47	1.92	0.46
	PAMILT^2	0.86	0.84	1.87	0.98
SCK-CEN	LSAPC	0.16	0.07	1.00	0.80
	PAMILT^1	0.21	0.12	1.11	0.73
	PAMILT^2	0.86	0.80	1.34	0.99

3.2. Sensitivity analysis

3.2.1. Sensitivity analysis with respect to meteorological inputs

Figure 6 compares the results for ETEX-I with three different types of meteorological input data. The maximal model biases in each case have similar ranges, but the spatial distributions are different. PAMILT reduces the maximal model biases to different degrees for the three cases, with respect to both the spatial distribution and the statistics in the lower-left corner (Fig. 6D–F). The LSAPC estimates exhibit oscillations of varying degrees in the release windows of the three cases, with the release rates deviating from the true values by up to −99.52% (underestimation) and up to 66.82% (overestimation). Additionally, LSAPC produces a noticeable artificial peak release at time zero for ERA-Interim A (indicated by the arrow in Fig. 6H). In contrast, the PAMILT profiles match the true release profiles closely, with deviations of less than 24.60% in the release window. For ERA-40 A and ERA-Interim B, PAMILT recovers both the sharp changes and steady phase of the release, and the end time of the release matches the true profile exactly for ERA-Interim B. For ERA-Interim A (Fig. 6H), the PAMILT profile shows some slight distortion, but there is no artificial peak at time zero and no oscillations in the release window. As for the total release, LSAPC produces underestimations of 32.42–79.70%, whereas the errors of PAMILT are at most 13.19%, indicating that PAMILT can achieve steady performance with different meteorological inputs.

Besides, the ERA-Interim B case (Fig. 6I) was also used to validate an upgraded LSAPC method (LSAPC with a bias correction function, i.e. BiasCorr-LSAPC) in a very recent study [11]. Yet, the BiasCorr-LSAPC methods still show residual oscillations and artificial release outside the release window (the second and third row of Fig. 6 in the reference [11]), whereas both errors have been corrected in the PAMILT result (Fig. 6I).

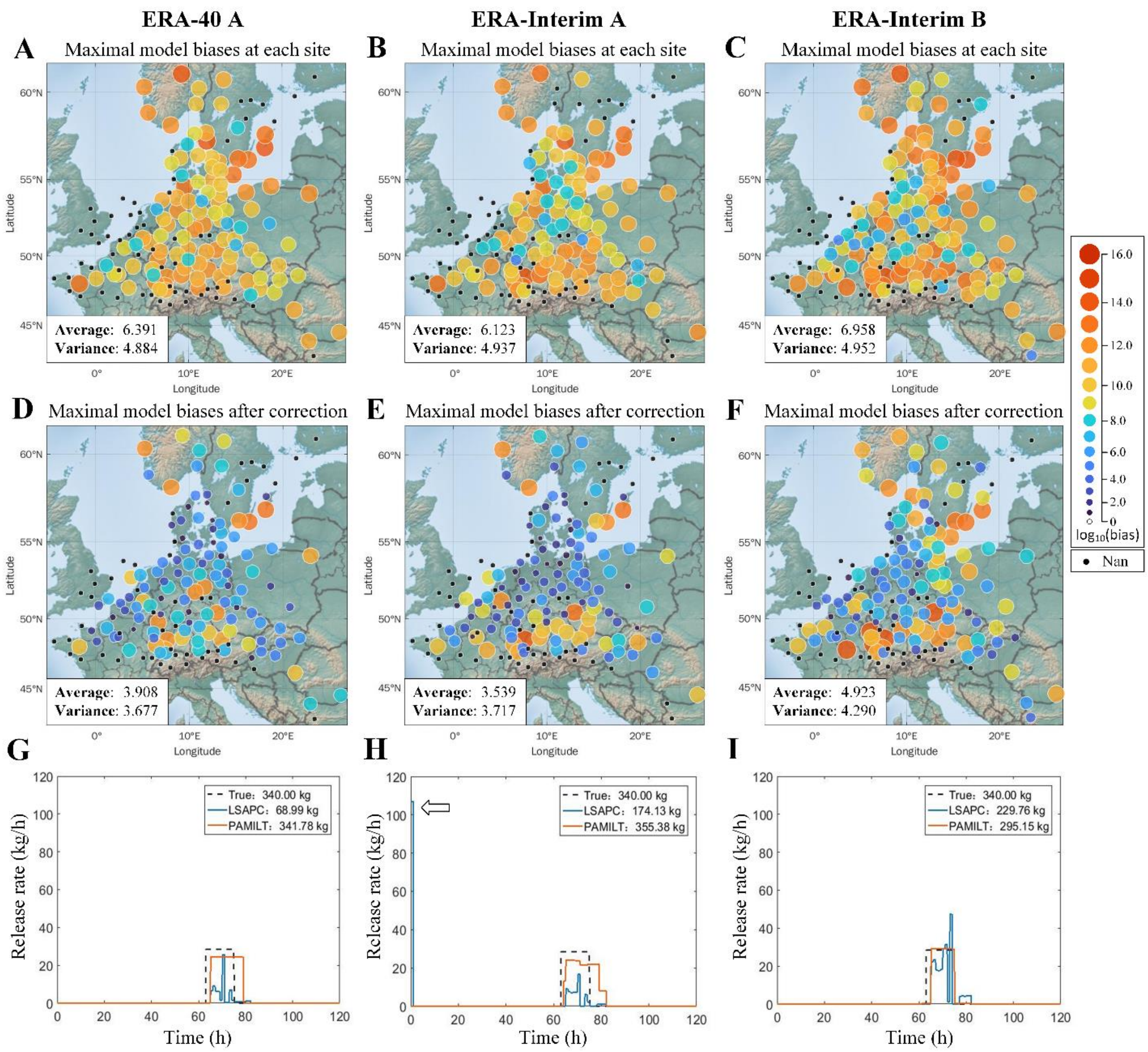

Figure 6. Inversion results for the ETEX-I experiment using different meteorological inputs: (left) ERA-40 A, (middle) ERA-Interim A, and (right) ERA-Interim B. (A)–(C) Maximal model biases at each site before correction; (D)–(F) maximal model biases at each site after PAMILT correction; (G)–(I) LSAPC and PAMILT estimated profiles.

3.2.2. Sensitivity analysis with respect to the number of observation sites

Figure 7 displays the representative temporal profiles estimated using 12.5%, 25%, 50%, and 75% of the observation sites for ERA-40 B. The LSAPC profiles exhibit oscillations in the release window and artificial releases outside the window for all cases, deviating from the true profile. In contrast, the PAMILT profile is free of oscillations and the shapes are close to the true profile, recovering both the sharp changes and steady phase. Additionally, PAMILT avoids artificial releases outside the release window. With fewer sites, the PAMILT profiles indicate earlier endpoints of the release than the ground truth. As the number of sites increases, PAMILT provides a more accurate end time, agreeing with the ground truth. With respect to the total release, PAMILT gives underestimations exceeding 30.82% with 12.5% or 25.0% sites. When 50% or more sites are considered, PAMILT provides more stable total release estimates, with deviations of less than 14.90% from the ground truth. Therefore, PAMILT achieves robust performance with respect to the number of observation sites.

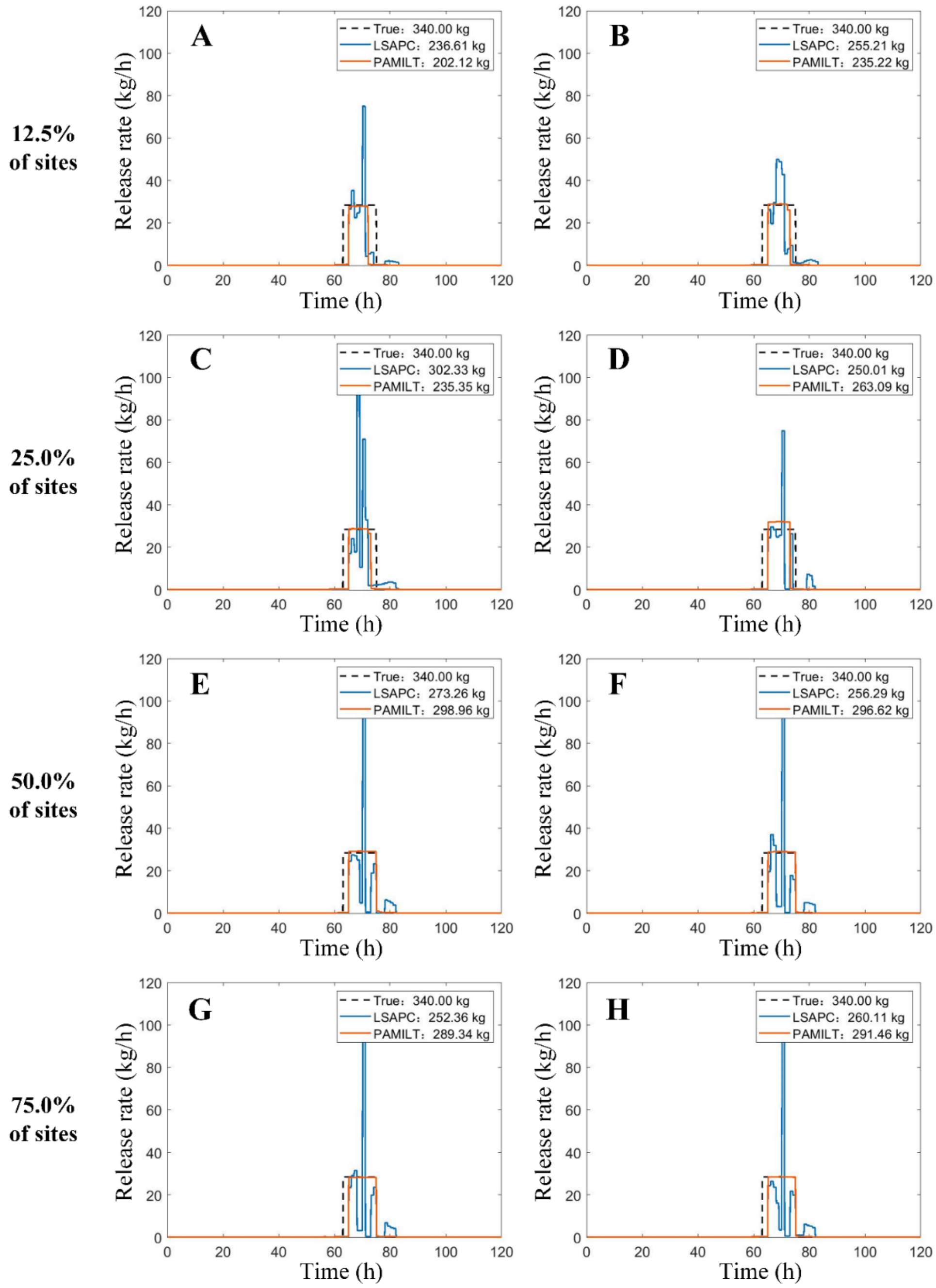

Figure 7. Inversion results using partial observation sites for the ETEX-I ERA-40 B case. (A), (B) 12.5% of the observation sites; (C), (D) 25% of the observation sites; (E), (F) 50% of the observation sites; (G), (H) 75% of the observation sites. Each row presents two different cases involving the same number of randomly selected sites.

3.2.3. Effect of the regularization parameter

Figure 8 displays the relative inversion error of PAMILT with different $\boldsymbol{\lambda}$. The relative error curves are generally quite typical for regularization methods, indicating that many existing algorithms may be applied for optimal parameter selection [31]. For ETEX-I ERA-40 B (Fig. 8A) and CAPTEX (Fig. 8B), the relative error curves show a rapid decrease as $\boldsymbol{\lambda}$ increases. After reaching the minimum, the relative errors increase smoothly and reach a steady state. For SCK-CEN (Fig. 8C), the enlarged view illustrates the error behavior at small $\boldsymbol{\lambda}$, as the inversion error starts from a lower value than in the other two experiments. Although two regularization terms are involved, the relative inversion error of three real cases varies smoothly with the regularization parameter, enabling optimal selection of the regularization parameter.

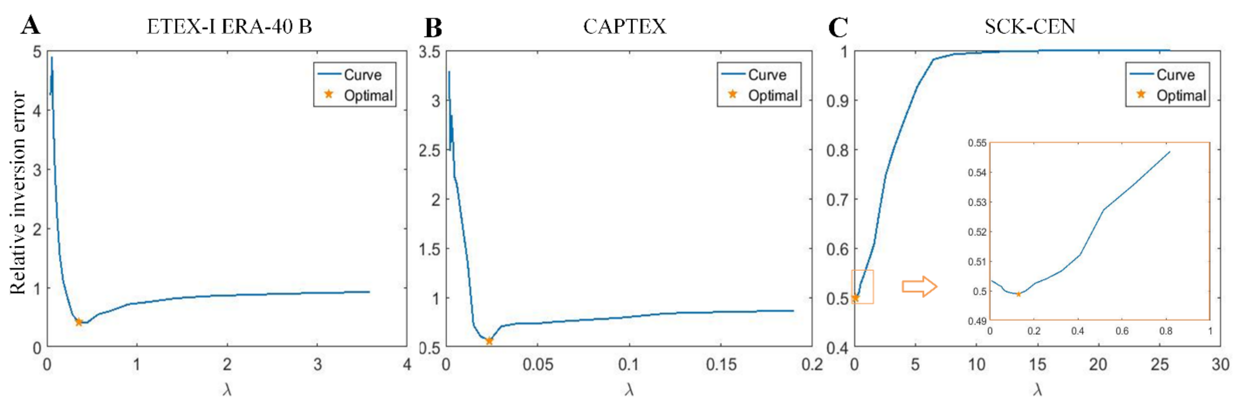

Figure 8. Relative inversion error of PAMILT for three field experiments with different values of the regularization parameter λ. (A) ETEX-I ERA-40 B; (B) CAPTEX; (C) SCK-CEN. The yellow stars denote the optimal values.

3.2.4. Competing effect of the two regularization terms

As shown in Fig. 9A, with $\alpha \leq 0.01$, the TV term dominates the model behavior, leading to a prolonged-release window and overestimated release rates. As α increases, the sparsity promotion effect of the L1-norm term gradually appears, significantly reducing the artificial releases outside the true release window. Further increasing α reduces the release rate and shortens the release window, leading to underestimated total releases. However, the shape of the release profile remains similar to the true profile. Based on the results in Fig. 9, α is set to 0.1 in all the test cases in this study.

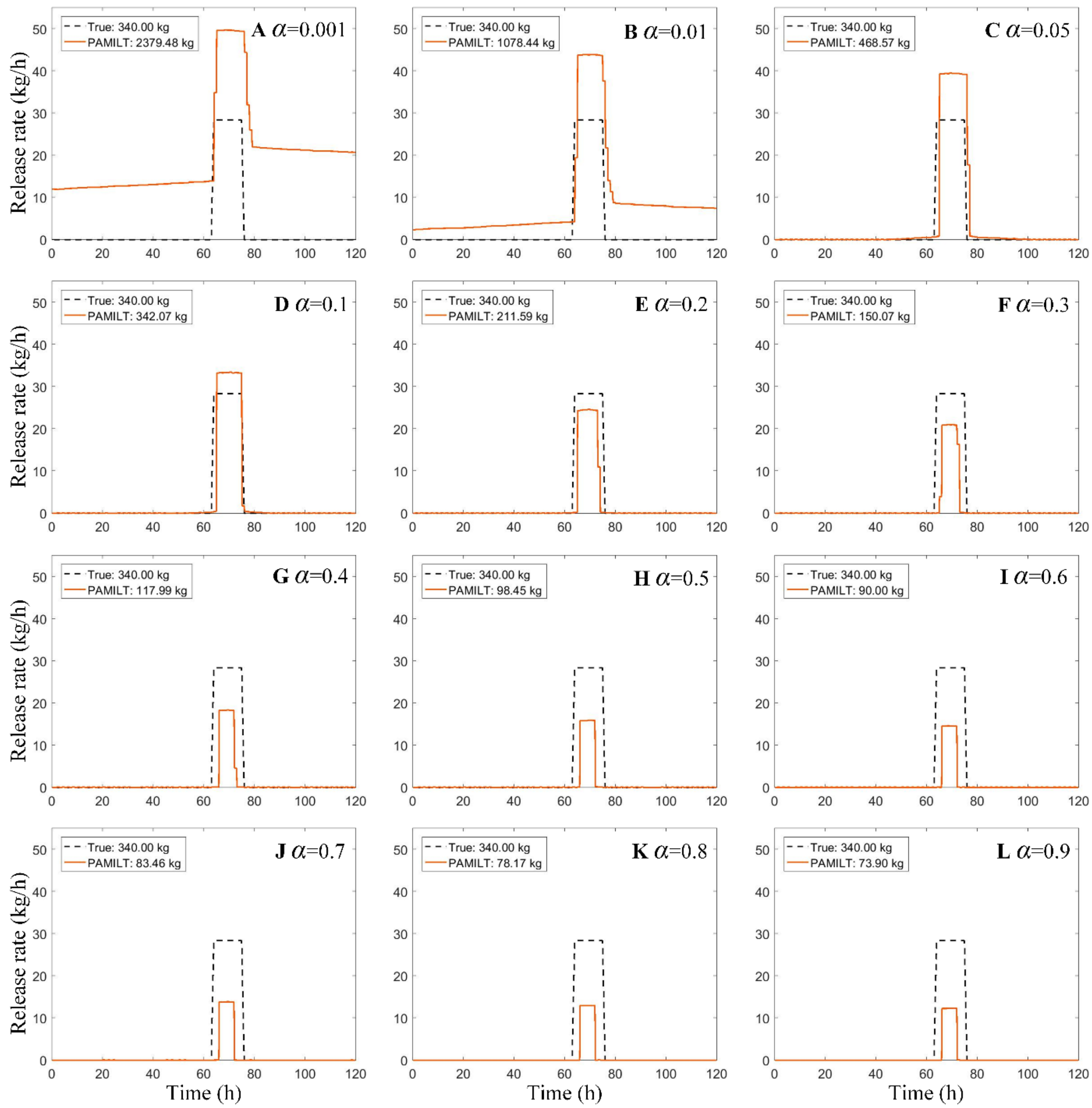

Figure 9. Comparison of PAMILT estimates for the ETEX-I ERA-40 B case using different values of $\boldsymbol{\alpha}$ from 0.1 to 0.9.

3.2.5. Center constraint value of correction coefficients

Figure 10 displays the relative inversion error of different center constraint values. As the center constraint value increases, the relative error curve first drops to a minimum at 0.001 and then increases again.

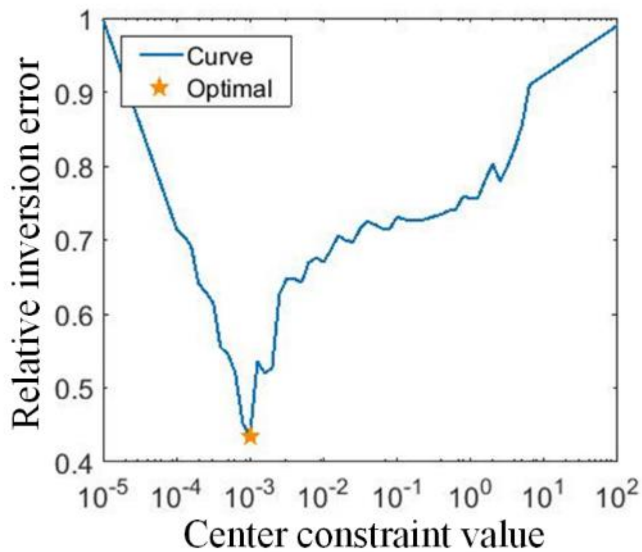

Figure 10. Relative inversion error of PAMILT using different center constraints for the ETEX-I ERA-40 B case.

Figure 11 compares the distributions of the correction coefficients estimated using different center constraint values with the true model biases. The center constraint value influences not only the range of estimates but also the shape of the distribution. As the center constraint value decreases, the high-frequency parts of the two distributions initially exhibit an increasing degree of overlap and agreement. When the center constraint value exceeds 0.001, the overlap begins to decrease, which is consistent with the tendency in Fig. 10.

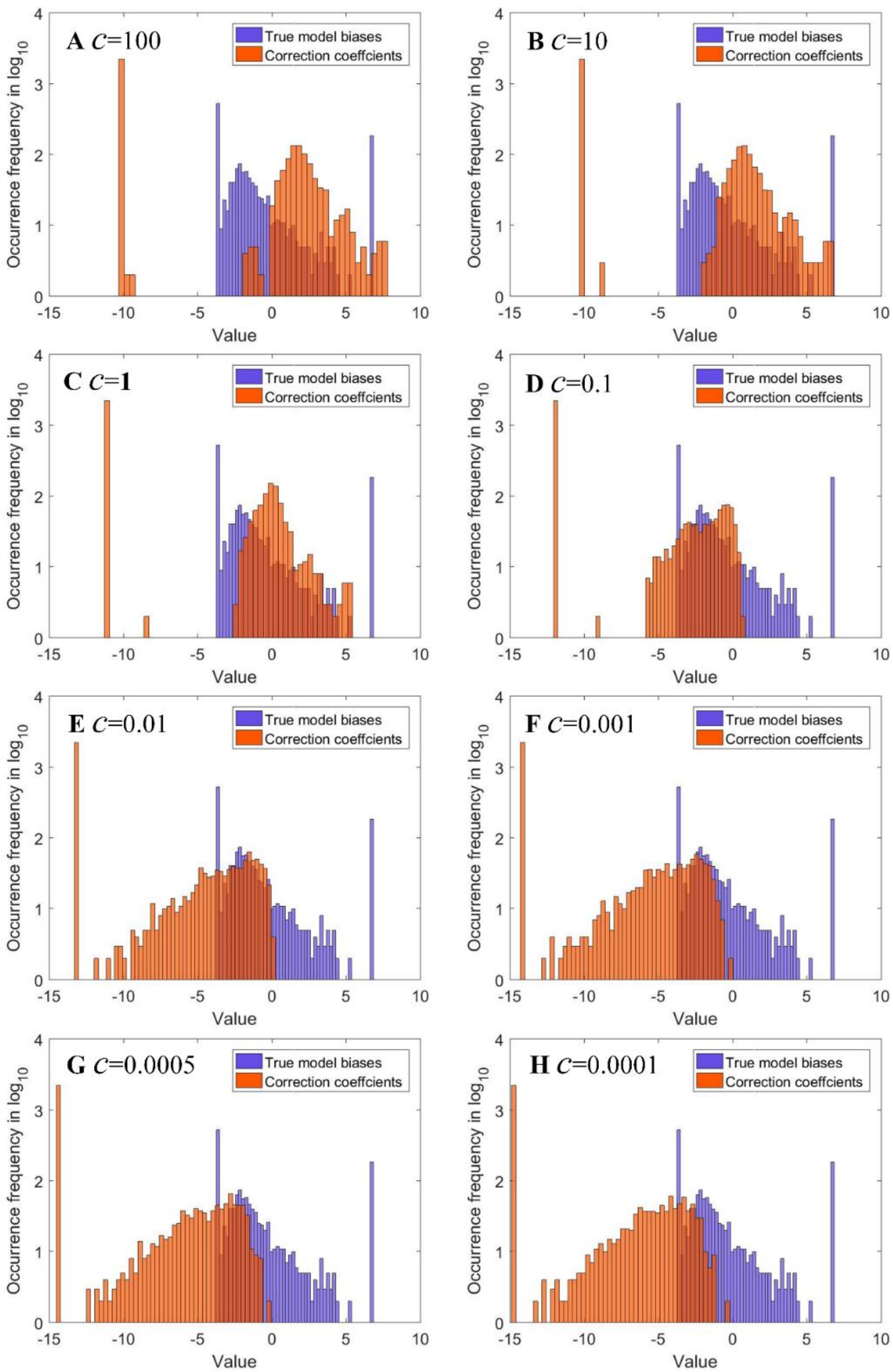

Figure 11. Distribution of the correction coefficients estimated using different center constraints ***c*** for the ETEX-I ERA-40 B case.

Figure 12 displays the estimated release profiles corresponding to Fig. 11. Larger center constraint values (Fig. 12A–E) lead to flatter release profiles, featuring underestimated release rates and overestimated release windows. Decreasing the center constraint increases the release rate and simultaneously shortens the release window, leading to a profile that is closer to the true profile. Further decreasing the center const raint leads to underestimated total releases and overestimated release rates in the steady state.

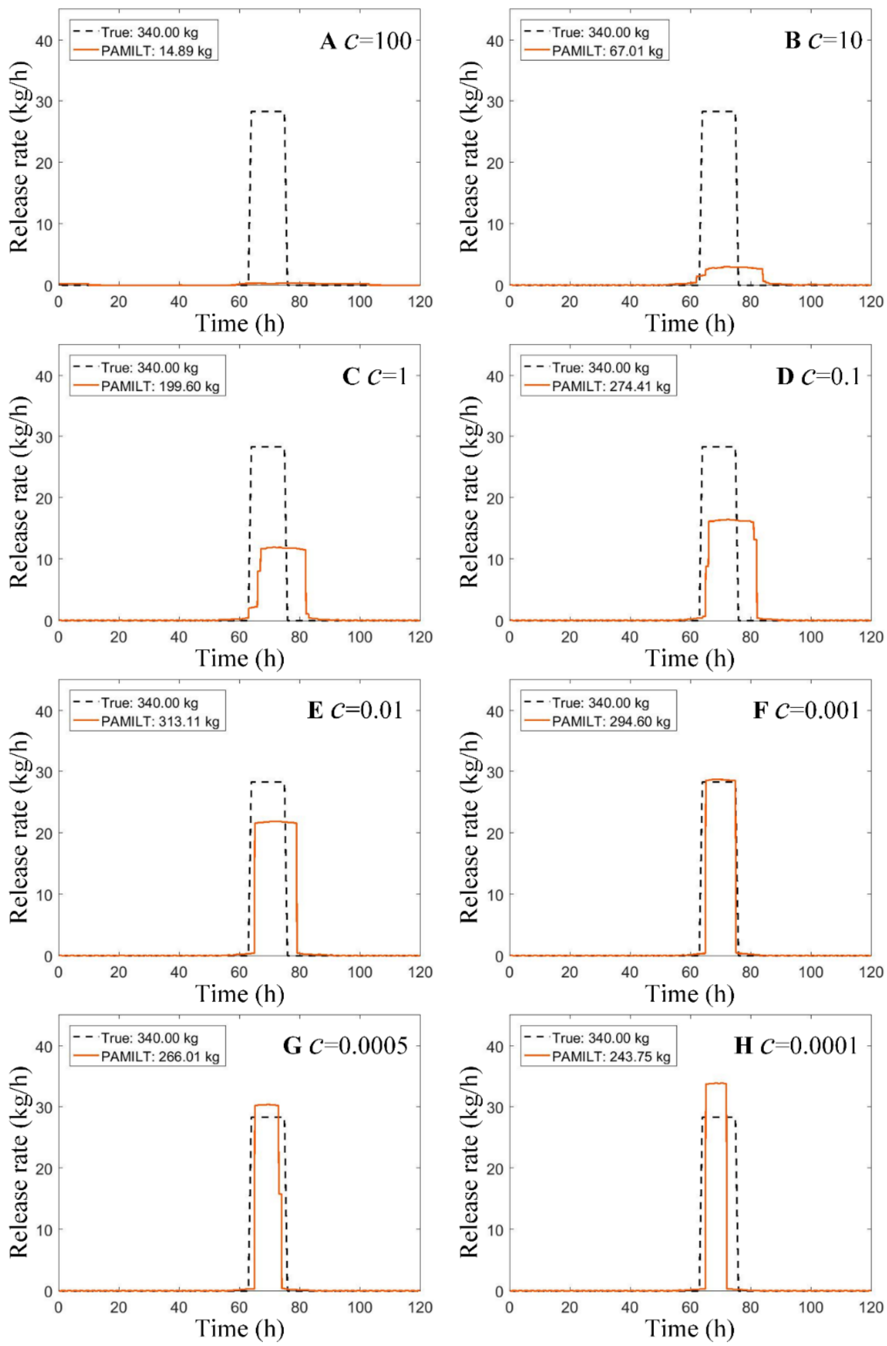

Figure 12. Comparison of estimates using different center constraints c for the ETEX-I ERA-40 B case.

3.3. Roles of each component in PAMILT

Figure 13 compares the release profile estimated using different components of PAMILT for the ERA-40 B case. Inversion using only TV (Fig. 13A) or TV + L1-norm (Fig. 13B) regularization does not take the model uncertainties into consideration, and produces stage-like variations in the release rates and artificial releases outside the window. Without any regularization, the joint correction model alone cannot handle the observation uncertainties and the PAM solution exhibits considerably overestimated release rates and prolonged release windows (Fig. 13C). For TV-regularized PAM (PAM + TV), the estimated release profile exhibits overestimations of both the release rates and the release duration (Fig. 13D), but no oscillations. On the contrary, the L1-norm-regularized PAM (PAM + L1-norm) exhibits a very short release duration, leading to an underestimated release amount (Fig. 13E). With PAMILT, the TV and L1-norm terms counteract the negative effects of one another, achieving a solution that almost perfectly matches the true profile (Fig. 13F). With respect to the total release, the TV and TV + L1-norm regularized profiles show similar underestimations (about 24.2% and 31.1%, respectively). Both PAM and PAM + TV noticeably overestimate the total release, whereas PAM + L1-norm produces a significant underestimation. The combination of PAM, TV, and L1-norm (PAMILT) gives a total release that is very close to the true value, which efficiently handles both the model biases and observation uncertainties.

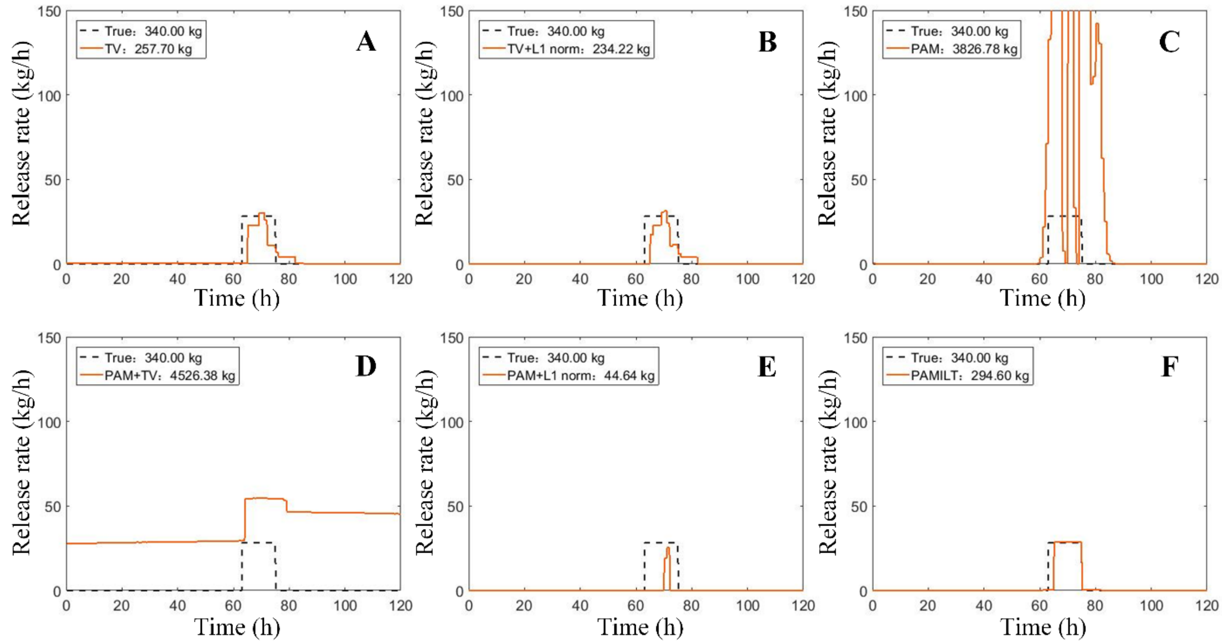

Figure 13. Comparison of estimates for the ETEX-I ERA-40 B case using different combinations of regularization terms and PAM. (A) Standard inversion + TV; (B) standard inversion + TV + L1-norm; (C) PAM; (D) PAM + TV; (E) PAM + L1-norm; (F) PAMILT.

3.4. Extension as a target-driven framework

The joint correction model, non-smooth priors (L1 and TV), and the new algorithm (tailored PAM) provide a fundamental framework for robust source term inversion, and achieve unprecedented (nearly perfect) inversion quality for both chemical and radioactive materials in three real emission cases at different scales. The framework has the flexibility to incorporate different inverse models and prior knowledge.

For instance, it would be straightforward to replace the joint correction model with the Simultaneous Estimation of the Release rate And Correction of both the plume range and Transport pattern (SERACT) model described in our previous study [7]. SERACT can overcome the inefficiency of the joint correction model in cases where the ADM simulation produces a zero output for a nonzero observation, and further improves the robustness of the framework. Similarly, the generality of the framework allows the use of other priors, especially the specific features of the emission. For example, a prior specifying the radionuclide composition can be employed to reconstruct the multi-radionuclide emissions of multiple radionuclides following nuclear accidents [14,32].

4. Conclusion

We have proposed an inversion method that returns oscillation-free and nearly perfect temporal release profiles of real emissions of the PMCH and radionuclide ^{41}Ar across different spatial scales. This method extends the joint correction model with a new regularization of two competing non-smooth priors, to compensate the large observation uncertainties and to recover fine release details in real cases. The two priors offset each other's side effects, of which the combination better models the unsteady and unsmooth feature of the radionuclide releases. This help distinguish the true releases from oscillations, enabling simultaneous oscillation removal and release recovery. A tailored algorithm is also designed for solving the regularized joint correction model. The multiscale validations against three real cases demonstrate that the proposed method achieves superior inversion quality to that of state-of-the-art algorithms, with improvements in the peak estimates, temporal window, and total release amount. The proposed method exhibits stable performance in the presence of different meteorological inputs and different numbers of observation sites. In addition, it requires only limited parameter tuning, indicating strong potential for operational usage. The proposed method shows that model biases and observation uncertainties can be efficiently handled through the combinational framework of the joint correction model, non-smooth competing priors, and the tailored projected alternating minimization algorithm. This framework can be applied to the inversion of diverse emissions at different scales, ranging from global to industrial park emissions.

Data and materials availability

Meteorological data, source–receptor matrices of ETEX- I, and FLEXPART-WRF model are available online as described in Materials and Methods. Note that the data that support the findings of this study are deposited in local storage at Tsinghua University. Additional scripts, codes, or data are available which may be requested from the authors upon reasonable request.

CRediT authorship contribution statement

Sheng Fang: Methodology, Investigation, Writing – original draft & review & editing, Formal analysis. **Xinwen Dong**: Methodology, Investigation, Writing – original draft & review & editing, Formal analysis. **Shuhan Zhuang**: Methodology, Investigation, Writing – original draft & review & editing, Formal analysis. **Zhijie Tian:** Data curation. **Tianfeng Chai:** Data curation, Formal analysis. **Yuhan Xu:** Formal analysis. **Yungang Zhao:** Investigation, Data curation. **Li Sheng:** Formal analysis. **Xuan Ye:** Resources, Supervision. **Wei Xiong:** Supervision, Funding acquisition.

Declaration of Competing Interest

The authors declare that they have no known competing financial interests or personal relationships that could have appeared to influence the work reported in this paper.

Acknowledgment

This work is supported by the National Natural Science Foundation of China [grant number 11875037] and International Atomic Energy Agency (TC project number CRP9053). We thank Adam, L. and Tichý, O. for kindly sharing the source-receptor matrices of the ETEX experiment and we thank Tichý, O. for sharing the code of LS-APC algorithm. We thank Bent Lauritzen, PhD, from Technical University of Denmark, for kindly providing the SCK-CEN field experiment data.

References

[1] A.A. Abagyan, L.A. Ilyin, Y.A. Izrael, V.A. Legasov, V.E. Petrov, The information on the Chernobyl accident and its consequences prepared for IAEA, Sov. At. Energy. 61 (1987) 301–320.

[2] Tokyo Electric Power Company (TEPCO), Estimation of Radioactive Material Released to the Atmosphere during the Fukushima Daiichi NPS Accident, 2012. http://www.tepco.co.jp/en/press/corp-com/release/betu12_ e/images/120524e0205.pdf (accessed May 21, 2022).

[3] O. Saunier, D. Didier, A. Mathieu, O. Masson, J. Dumont Le Brazidec, Atmospheric modeling and source reconstruction of radioactive ruthenium from an undeclared major release in 2017, Proc. Natl. Acad. Sci. U. S. A. 116 (2019) 24991–25000. https://doi.org/10.1073/pnas.1907823116.

[4] N. Evangeliou, S. Eckhardt, Uncovering transport, deposition and impact of radionuclides released after the early spring 2020 wildfires in the Chernobyl Exclusion Zone, Sci. Reports 2020 101. 10 (2020) 1–10. https://doi.org/10.1038/s41598-020-67620-3.

[5] X. Li, H. Li, Y. Liu, W. Xiong, S. Fang, Joint release rate estimation and measurement-by-measurement model correction for atmospheric radionuclide emission in nuclear accidents: An application to wind tunnel experiments, J. Hazard. Mater. 345 (2018) 48–62. https://doi.org/10.1016/j.jhazmat.2017.09.051.

[6] O. Tichý, V. Ŝmídl, R. Hofman, K. Ŝindelárová, M. Hýza, A. Stohl, Bayesian inverse modeling and source location of an unintended 131I release in Europe in the fall of 2011, Atmos. Chem. Phys. 17 (2017) 12677–12696. https://doi.org/10.5194/acp-17-12677-2017.

[7] S. Fang, S. Zhuang, X. Li, H. Li, Automated release rate inversion and plume bias correction for atmospheric radionuclide leaks: A robust and general remediation to

imperfect radionuclide transport modeling, Sci. Total Environ. 754 (2021). https://doi.org/10.1016/j.scitotenv.2020.142140.

[8] D. Pillai, C. Gerbig, R. Kretschmer, V. Beck, U. Karstens, B. Neininger, M. Heimann, Comparing Lagrangian and Eulerian models for CO 2 transport-a step towards Bayesian inverse modeling using WRF/STILT-VPRM, Atmos. Chem. Phys. 12 (2012) 8979–8991. https://doi.org/10.5194/acp-12-8979-2012.

[9] D.B. Ryall, R.H. Maryon, Validation of the UK Met. Office's name model against the ETEX dataset, Atmos. Environ. 32 (1998) 4265–4276. https://doi.org/10.1016/S1352-2310(98)00177-0.

[10] Y. Liu, J.M. Haussaire, M. Bocquet, Y. Roustan, O. Saunier, A. Mathieu, Uncertainty quantification of pollutant source retrieval: comparison of Bayesian methods with application to the Chernobyl and Fukushima Daiichi accidental releases of radionuclides, Q. J. R. Meteorol. Soc. 143 (2017) 2886–2901. https://doi.org/10.1002/qj.3138.

[11] O. Tichý, V. Šmídl, N. Evangeliou, Source term determination with elastic plume bias correction, J. Hazard. Mater. (2021) 127776. https://doi.org/10.1016/J.JHAZMAT.2021.127776.

[12] O. Tichý, V. Šmídl, R. Hofman, A. Stohl, LS-APC v1.0: A tuning-free method for the linear inverse problem and its application to source-Term determination, Geosci. Model Dev. 9 (2016) 4297–4311. https://doi.org/10.5194/gmd-9-4297-2016.

[13] A. Stohl, P. Seibert, G. Wotawa, D. Arnold, J.F. Burkhart, S. Eckhardt, C. Tapia, A. Vargas, T.J. Yasunari, Xenon-133 and caesium-137 releases into the atmosphere from the Fukushima Dai-ichi nuclear power plant: Determination of the source term, atmospheric

dispersion, and deposition, Atmos. Chem. Phys. 12 (2012) 2313–2343. https://doi.org/10.5194/acp-12-2313-2012.

[14] O. Saunier, A. Mathieu, D. Didier, M. Tombette, D. Quélo, V. Winiarek, M. Bocquet, An inverse modeling method to assess the source term of the Fukushima Nuclear Power Plant accident using gamma dose rate observations, Atmos. Chem. Phys. 13 (2013) 11403–11421. https://doi.org/10.5194/acp-13-11403-2013.

[15] H. Terada, H. Nagai, K. Tsuduki, A. Furuno, M. Kadowaki, T. Kakefuda, Refinement of source term and atmospheric dispersion simulations of radionuclides during the Fukushima Daiichi Nuclear Power Station accident, J. Environ. Radioact. 213 (2020) 106104. https://doi.org/10.1016/J.JENVRAD.2019.106104.

[16] V. Winiarek, M. Bocquet, O. Saunier, A. Mathieu, Estimation of errors in the inverse modeling of accidental release of atmospheric pollutant: Application to the reconstruction of the cesium-137 and iodine-131 source terms from the Fukushima Daiichi power plant, J. Geophys. Res. Atmos. 117 (2012). https://doi.org/10.1029/2012JD018107.

[17] V. Winiarek, M. Bocquet, N. Duhanyan, Y. Roustan, O. Saunier, A. Mathieu, Estimation of the caesium-137 source term from the Fukushima Daiichi nuclear power plant using a consistent joint assimilation of air concentration and deposition observations, Atmos. Environ. 82 (2014) 268–279. https://doi.org/10.1016/j.atmosenv.2013.10.017.

[18] L. Adam, M. Branda, Sparse optimization for inverse problems in atmospheric modelling, Environ. Model. Softw. 79 (2016) 256–266. https://doi.org/10.1016/j.envsoft.2016.02.002.

[19] M. Martinez-Camara, I. Dokmanic, J. Ranieri, R. Scheibler, M. Vetterli, A. Stohl, THE FUKUSHIMA INVERSE PROBLEM, in: ICASSP, IEEE Int. Conf. Acoust. Speech Signal Process. - Proc., 2013: pp. 4330–4334.

[20] T. Chai, R. Draxler, A. Stein, Source term estimation using air concentration measurements and a Lagrangian dispersion model - Experiments with pseudo and real cesium-137 observations from the Fukushima nuclear accident, Atmos. Environ. 106 (2015) 241–251. https://doi.org/10.1016/j.atmosenv.2015.01.070.

[21] G. Katata, M. Chino, T. Kobayashi, H. Terada, M. Ota, H. Nagai, M. Kajino, R. Draxler, M.C. Hort, A. Malo, T. Torii, Y. Sanada, Detailed source term estimation of the atmospheric release for the Fukushima Daiichi Nuclear Power Station accident by coupling simulations of an atmospheric dispersion model with an improved deposition scheme and oceanic dispersion model, Atmos. Chem. Phys. 15 (2015) 1029–1070. https://doi.org/10.5194/acp-15-1029-2015.

[22] N. Evangeliou, T. Hamburger, A. Cozic, Y. Balkanski, A. Stohl, Inverse modeling of the Chernobyl source term using atmospheric concentration and deposition measurements, Atmos. Chem. Phys. 17 (2017) 8805–8824. https://doi.org/10.5194/acp-17-8805-2017.

[23] D. Perrone, P. Favaro, Total variation blind deconvolution: The devil is in the details, in: Proc. IEEE Comput. Soc. Conf. Comput. Vis. Pattern Recognit., 2014: pp. 2909–2916. https://doi.org/10.1109/CVPR.2014.372.

[24] K. Nodop, R. Connolly, F. Girardi, The field campaigns of the European tracer experiment (ETEX): Overview and results, Atmos. Environ. 32 (1998) 4095–4108. https://doi.org/10.1016/S1352-2310(98)00190-3.

[25] G.J. Ferber, J.L. Heffter, R.R. Draxler, R.J. Lagomarsino, F.L. Thomas, R.N. Dietz, C.M. Benkovitz, Cross-appalachian tracer experiment (CAPTEX ’83) final report, 1986.

[26] M. Drews, H.K. Aage, K. Bargholz, H. Ejsing Jørgensen, U. Korsbech, B. Lauritzen, T. Mikkelsen, C. Rojas-Palma, R. Van Ammel, Measurements of plume geometry and argon-41 radiation field at the BR1 reactor in Mol, Belgium, 2002.

[27] M. Martinez-Camara, M. Vetterli, A. Stohl, Outlier removal for improved source estimation in atmospheric inverse problems, in: ICASSP, IEEE Int. Conf. Acoust. Speech Signal Process. - Proc., 2014: pp. 6820–6824. https://doi.org/10.1109/ICASSP.2014.6854921.

[28] A. Levin, Y. Weiss, F. Durand, W.T. Freeman, Efficient marginal likelihood optimization in blind deconvolution, Proc. IEEE Comput. Soc. Conf. Comput. Vis. Pattern Recognit. (2011) 2657–2664. https://doi.org/10.1109/CVPR.2011.5995308.

[29] R. Addis, G. Fraser, F. Girardi, G. Graziani, Y. Inoue, N. Kelly, W. Klug, A. Kulmala, K. Nodop, J. Pretel, ETEX: a European tracer experiment; observations, dispersion modelling and emergency response, Atmos. Environ. 32 (1998) 4089–4094.

[30] X. Li, W. Xiong, X. Hu, S. Sun, H. Li, X. Yang, Q. Zhang, M. Nibart, A. Albergel, S. Fang, An accurate and ultrafast method for estimating three-dimensional radiological dose rate fields from arbitrary atmospheric radionuclide distributions, Atmos. Environ. 199 (2019) 143–154. https://doi.org/10.1016/j.atmosenv.2018.11.001.

[31] P.C. Hansen, Rank-deficient and discrete ill-posed problems: numerical aspects of linear inversion, Society for Industrial and Applied Mathematics, 1998.

[32] X. Li, S. Sun, X. Hu, H. Huang, H. Li, Y. Morino, S. Wang, Source inversion of both long- and short-lived radionuclide releases from the Fukushima Daiichi nuclear accident using on-site gamma dose rates, J. Hazard. Mater. 379 (2019) 120770. https://doi.org/10.1016/j.jhazmat.2019.120770.

631